# Sensorless Control of Doubly-Fed Induction Generators Based on Rotor High Frequency Signal Injection

David Reigosa, Fernando Briz, Cristian Blanco, †Antonio Di Gioia, Pablo García, Juan Manuel Guerrero
University of Oviedo. Dept. of Elect., Computer & System Engineering. Gijón, 33204 Spain. reigosa@isa.uniovi.es, fernando@isa.uniovi.es, blancocristian@uniovi.es, pgarcia@isa.uniovi.es, guerrero@isa.uniovi.es
University of Rome, "la Sapienza", a_digio@hotmail.it

**Abstract: This paper analyzes the use of high frequency signal injection methods for the sensorless control of doubly-fed induction generators (DFIG). High frequency signal injection methods have been widely investigated for the sensorless control at very low speed and position control of induction machines (IM) and permanent magnet synchronous machines (PMSM). Most of these methods inject a high frequency voltage signal in the stator windings, which interacts with the machine asymmetries (saliencies), modulating the resulting stator high frequency currents, from which the rotor position is estimated. The use of these methods with doubly-fed induction generators (DFIG) is studied in this paper, with special focus on two distinguishing features compared to the case of other types of three-phase machines: 1) it is feasible to inject the high frequency signal in the rotor, since the rotor windings are accessible and 2) as a consequence of this, it is possible to use the method with non-salient machines.[1]**

**Index Terms— DFIG, high frequency signal injection, sensorless control.**

## I. Introduction

The installed wind power capacity has grown quickly during the last years [1]. China has installed 16.500MW in 2010 for an accumulated power of 42.287MW, US has already gone over 40.000MW, with Germany, Spain and India being third, fourth and fifth with 27.214, 20.676 and 13.065MW respectively [1]. In countries like Spain, wind power covers 16.4% of the overall electricity demand [1,2], which places this technology as the third contributor behind combined cycle and nuclear. This tendency is expected to continue during the next years, the National Renewable Energy Action Plan of the Spanish government foreseeing to reach 35.000MW of on-shore and 3.000MW of off-shore installed power in 2020 [1,3].

Due to the increase of the wind energy penetration, the requirements to system operators in terms of operation and connection reliability has become more restrictive [3-8], often being similar to those for conventional power plants, including ride through and grid support capabilities [6].

DFIG's are of great importance for wind power generation. On-shore wind power systems based on DFIG's applications, accounts for around 50% of the installed wind turbines all over the world [4]. Wind power generation using DFIG's have several appealing properties:

- Compared to other machine designs like IM and PMSM, the size of the power converter is only a fraction of the machine power [9, 10], assumed that the power converter feeds the rotor, and the stator connected directly to the line, therefore reducing the overall cost.
- Active and reactive power can be independently controlled [11].
- Can operate both below and above of synchronous speed [11].
- By controlling the machine speed (variable frequency), maximum power point tracking strategies, as well as ride trough strategies can be implemented, improving both the quantity as well as the quality of the energy injected to the network [11].

Control of DFIG's has been the focus of significant research efforts during the last years mainly due to their use in wind power generation systems. One field of special interest is sensorless control. The elimination of the position/speed sensor, as well as of its associated cabling and connectors being attractive as this reduces the number of elements which are susceptible of failure, as well as the cost of the overall system. While a large amount of work has been published on the sensorless control of PMSM's and IM's [17-31], much less attention has been paid to the case of DFIG's [12-15].

Sensorless control of AC machines, PMSM's and IM's in the mid-high speed region based on the fundamental model of the machine has been widely studied and is commercially available [17, 18]. However, the performance of these methods decreases with the speed as they are primarily base on the back-emf, and can not be therefore used at very low or zero speed. To overcome these limitations, methods based on the injection of a high frequency excitation [19-31] have been proposed for the low speed range and position control. In these techniques, the interaction between the injected high frequency signal (normally a voltage) and the machine saliencies, modulates the resulting high frequency currents, from which the rotor

[1] This work was supported in part by the Research, Technological Development and Innovation Programs of the Spanish Ministry of Science and Innovation-ERDF under grant MICINN-10-ENE2010-14941 and the Ministry of Science and Innovation under grant MICINN-10-CSD2009-00046.

position can be extracted [19-31]. The high frequency signals can be obtained either from the PWM commutations [19, 21] or by adding some form of small magnitude, high frequency signal voltage to the fundamental excitation [22-32], e.g. rotating [22-27, 30, 31], pulsating [24, 26, 31] and square-wave [27,28] wave shapes. The rotor position is obtained by signal processing of the resulting stator high frequency current.

In a DFIG, the stator terminals normally are directly connected to the grid, while the rotor terminals are available (see Fig. 1). This produces significant differences in the implementation of the method compared to other types of three-phase AC machines, also opening interesting opportunities. In the method proposed in this paper, a high frequency signal voltage is injected in the rotor using the power converter. The high frequency voltage induced in the stator will be shown to be modulated by the rotor angle, from which it is possible to estimate the rotor position.

The paper is organized as follow: the high frequency model of the DGIF and the physical principles of the method are presented in Sections II and III; implementation issues are introduced in Section IV; finally, simulation and experimental results to confirm the viability of the method are provided in Sections V and VI respectively.

## II. High frequency model of a DFIG

The model of a DFIG in a stationary *qd*-reference frame, is given by (1)-(8) [34].

$$v_{ds}^{s} = r_s i_{ds}^{s} + (L_{ls} + L_m)\frac{di_{ds}^{s}}{dt} - \omega_e (L_{ls} + L_m) i_{qs}^{s} + L_m \frac{di_{dr}^{s'}}{dt} - \omega_e L_m i_{qr}^{s'} \quad (1)$$

$$v_{qs}^{s} = r_s i_{qs}^{s} + (L_{ls} + L_m)\frac{di_{qs}^{s}}{dt} + \omega_e (L_{ls} + L_m) i_{ds}^{s} + L_m \frac{di_{qr}^{s'}}{dt} + \omega_e L_m i_{dr}^{s'} \quad (2)$$

$$v_{dr}^{s'} = r_r' i_{ds}^{s} + (L_{lr}' + L_m)\frac{di_{dr}^{s'}}{dt} + L_m \frac{di_{ds}^{s}}{dt} - -(\omega_e - \omega_r) L_m i_{qs}^{s} - (\omega_e - \omega_r)(L_{lr}' + L_m) i_{qr}^{s'} \quad (3)$$

$$v_{qr}^{s'} = r_r' i_{qs}^{s} + (L_{lr}' + L_m)\frac{di_{qr}^{s'}}{dt} + L_m \frac{di_{qs}^{s}}{dt} + +(\omega_e - \omega_r) L_m i_{ds}^{s} + (\omega_e - \omega_r)(L_{lr}' + L_m) i_{dr}^{s'} \quad (4)$$

$$r_r' = (N_s/N_r)^2 r_r \quad (5)$$

$$L_{lr}' = (N_s/N_r)^2 L_r \quad (6)$$

$$i_{qdr}^{s'} = (N_s/N_r) i_{qdr}^{s} \quad (7)$$

$$v_{qdr}^{s'} = (N_s/N_r) v_{qdr}^{s} \quad (8)$$

where $r_s$ is the stator resistance, $r_r'$ is the rotor resistance referred to the stator, $L_{ls}$ is the stator leakage inductance, $L_{lr}'$ is the rotor leakage inductance referred to the stator, $L_m$ is the magnetizing inductance, $N_s$ is the stator number of turns, $N_r$ is the rotor number of turns, $\omega_e$ is the stator frequency –line frequency–, $\omega_r$ is the rotor speed, $i_{qds}^{s}$ is the stator current complex vector, $i_{qdr}^{s'}$ is the rotor current complex vector referred to the stator, $v_{qds}^{s}$ is the stator voltage complex vector and $v_{qdr}^{s'}$ is rotor voltage complex vector referred to the stator, the transformation from three-phase quantities to *qd* quantities being (9).

$$f_{qd} = 2/3 * \left( f_a + f_b * e^{j*2*\pi/3} + f_c * e^{j*4*\pi/3} \right) \quad (9)$$

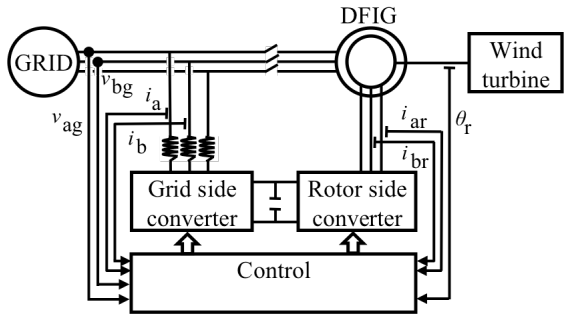


Fig. 1 Simplified wind energy conversion system using a DFIG.

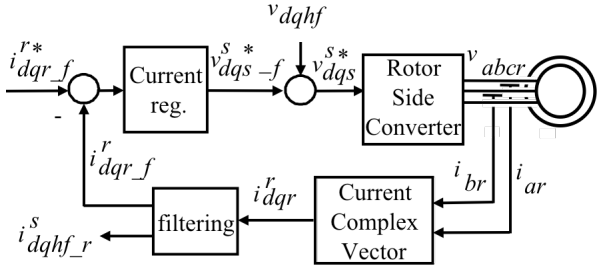


Fig. 2 Simplified block diagram showing the high frequency signal injection, current regulation and filtering.

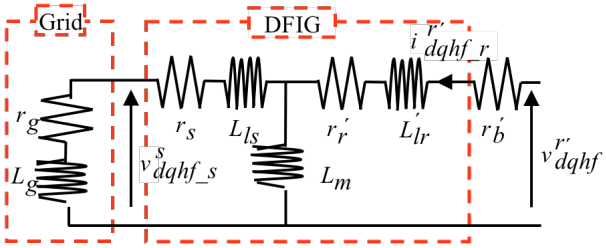


Fig. 3 High frequency models of the grid (referred to the stator), DFIG and rotor brushes.

If the rotor of the machine is fed with a high frequency voltage signal (see Fig. 1 and 2) and assuming that the frequency of the high frequency signal is significantly higher than the fundamental frequency and rotor speed (i.e. $\omega_{hf} >> \omega_e$ and $\omega_{hf} >> \omega_r$), the terms depending on the rotor speed and fundamental frequency in (1)-(4) can be safely neglected, the high frequency model shown in (10)-(13) being obtained, which is schematically represented in Fig. 3.

$$v_{ds}^{s} = r_s i_{ds}^{s} + (L_{ls} + L_m)\frac{di_{ds}^{s}}{dt} + L_m \frac{di_{dr}^{s'}}{dt} \quad (10)$$

$$v_{qs}^{s} = r_s i_{qs}^{s} + (L_{ls} + L_m)\frac{di_{qs}^{s}}{dt} + L_m \frac{di_{qr}^{s'}}{dt} \quad (11)$$

$$v_{dr}^{s'} = r_r' i_{ds}^{s} + (L_{lr}' + L_m)\frac{di_{dr}^{s'}}{dt} + L_m \frac{di_{ds}^{s}}{dt} \quad (12)$$

$$v_{qr}^{s'} = r_r' i_{qs}^{s} + (L_{lr}' + L_m)\frac{di_{qr}^{s'}}{dt} + L_m \frac{di_{qs}^{s}}{dt} \quad (13)$$

## III. High frequency signal injection and rotor position estimation

High frequency signal injection sensorless methods add some form of high frequency signal to the fundamental excitation command coming from the current regulator (see Fig. 2). Different types of periodic high frequency signals have been proponed in the literature, the most popular choices being rotating (14) [22-26, 29, 30], sinusoidal pulsating (15) [24, 26, 31] and square-wave (16) [27,28] signals. While all of them respond to the same physical principles and can potentially provide therefore the same performance, some differences exist in their practical implementation. The analysis following will use a rotating high frequency signal voltage (14), as the signal processing for this type of excitation is considered simpler. It is noted that the analysis and conclusions could easily be extended to other types of periodic excitation like pulsating (15) or square-wave (16).

$$v_{dqhf}^{r} = V_{hf} e^{j\omega_{hf} t} \quad (14)$$

$$v_{dqhf}^{r} = V_{hf}\cos(\omega_{hf} t) = \frac{V_{hf}}{2} e^{j(\omega_{hf} t)} + \frac{V_{hf}}{2} e^{j(-\omega_{hf} t)} \quad (15)$$

$$v_{dqshf}^{r} = \frac{4V_{hf}}{\pi} \sum_{h=1,3,5,\ldots}^{\infty} \frac{1}{2h-1} \sin\left[(2h-1)\omega_{hf} t + \pi\right] \quad (16)$$

where $\omega_{hf}$ is the frequency of the injected signal and $V_{hf}$ is the voltage magnitude of the injected high frequency signal.

If a rotating high frequency voltage signal (14) is injected in the rotor terminals of a DFIG (see Fig. 1 and 2), and assuming that the rotor speed and/or the fundamental excitation frequency change relatively slowly compared to the high frequency signal, -i.e. the machine can be assumed to operate in steady state-, the resulting high frequency rotor current (15) can be obtained from (10)-(14) (see Fig. 3), with the rotor high frequency impedance being (16) and the high frequency voltage vector induced in the stator terminals being (17).

$$i_{dqhf\_r}^{r} = \frac{V_{hf}}{\left|Z_{hf}^{r}\right|} e^{j(\omega_{hf} t - \varphi_{Z_{hf}^{r}})} \quad (15)$$

$$Z_{hf}^{r} = (r_r' + r_b') + j\omega_{hf} L_{lr}' + \frac{j(\omega_{hf} \pm \omega_r) L_m \left[(r_s + r_g) + j(\omega_{hf} \pm \omega_r)(L_{ls} + L_g)\right]}{(r_s + r_g) + j(\omega_{hf} \pm \omega_r)(L_{ls} + L_g)} \quad (16)$$

$$v_{dqhf\_s}^{s} = \frac{V_{hf}}{\left|Z_{hf}^{r}\right|}(r_g + j(\omega_{hf} \pm \omega_r) L_g) \frac{j(\omega_{hf} \pm \omega_r) L_m}{(r_s + r_g) + j(\omega_{hf} \pm \omega_r)(L_{ls} + L_g + L_m)} e^{j(\omega_{hf} t \pm \varphi_r - \varphi_{Z_{hf}^{r}})} \quad (17)$$

where $\left|Z_{hf}^{r}\right|$ is the magnitude of the rotor high frequency impedance ($Z_{hf}^{r}$), $\varphi_{Z_{hf}^{s}}$ is the phase of the rotor high frequency impedance, $r_b'$ is the brushes resistance referred to the stator ($r_b' = (N_s/N_r)^2 r_b$) and $\omega_r$ is the rotor speed.

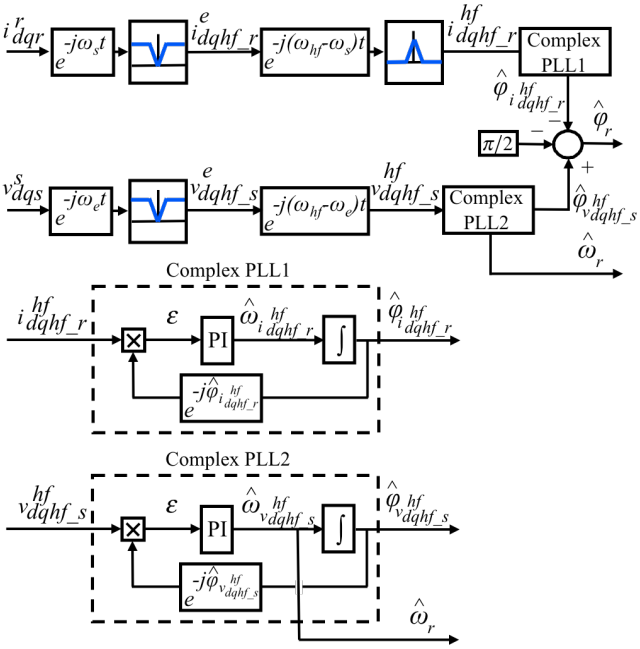


Fig. 4 Block diagram of the signal processing used for rotor position estimation. $\omega_s$ =slip frequency.

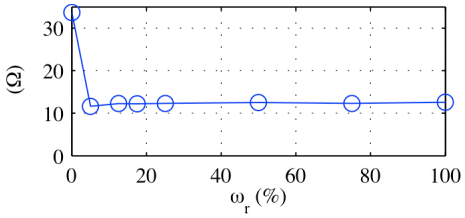


Fig. 5 High frequency brushes resistance. $\omega_{hf}$=2kHz.

Assuming that $(r_s + r_g) << (\omega_{hf} \pm \omega_r)(L_{ls} + L_g + L_m)$ and $r_g << (\omega_{hf} \pm \omega_r) L_g$, which is realistic given the inductive behavior of the machine and the large value of $\omega_{hf}$, the induced stator high frequency voltage, (17), can be simplified to (18).

$$v_{dqhf\_s}^{s} = \frac{V_{hf}}{\left|Z_{hf}^{r}\right|}(\omega_{hf} \pm \omega_r) L_g \frac{L_m}{(L_{ls} + L_g + L_m)} e^{j(\omega_{hf} t \pm \varphi_r - \varphi_{Z_{hf}^{r}} + \frac{\pi}{2})} \quad (18)$$

It can be observed from (15) and (18) that the phase angle between the rotor high frequency current complex vector ($i_{dqhf\_r}^{r}$) and the resulting stator high frequency voltage

complex vector ( $v^{s}_{dqhf\_s}$ ) is $\pi/2 \pm \varphi_r$ . It is possible therefore to estimate the rotor position $\hat{\varphi}_r$ from these two quantities.

The block diagram showing the signal processing needed to estimate the rotor position is shown in Fig. 4, with the inputs being the measured rotor current vector ( $i^{r}_{dqr}$ ) and the measured stator voltage vector ( $v^{s}_{dqs}$ ). It is noted that both signals are normally available in a DFIG [4, 10, 11, 16] for control and synchronization purposes. The filtering shown in Fig, 4 works as follow:

- The phase angle of the high frequency rotor current vector $\varphi_{i^{r}_{dqhf\_r}}$ is obtained from the measured rotor current complex vector after a filtering process and a complex PLL, while the phase of the resulting stator high frequency voltage complex vector ( $\varphi_{v^{hf}_{dqhf\_s}}$ ) is obtained from the stator voltage complex vector after removing the fundamental component by a filtering process and a complex PLL.
- The input to both complex PLLs, i.e. the high frequency components of the stator voltage vector, $v^{hf}_{dqhf\_s}$ (19) and of the rotor current vector, $i^{hf}_{dqhf\_r}$ (20), are obtained after removing the fundamental components from the measured signals, which is achieved using band-rejection filters (see Fig. 4).

$$v^{hf}_{dqhf\_s} = \frac{V_{hf}}{\left|Z^{r}_{hf}\right|}(\omega_{hf} \pm \omega_r)L_g \frac{L_m}{(L_{ls}+L_g+L_m)} e^{j(\pm\varphi_r - \varphi_{Z^{r}_{hf}} + \frac{\pi}{2})} \tag{19}$$

$$i^{hf}_{dqhf\_r} = \frac{V_{hf}}{\left|Z^{r}_{hf}\right|} e^{j(-\varphi_{Z^{r}_{hf}})} \tag{20}$$

- The resulting high frequency components are then rotated to the high frequency signal synchronous reference frame. The error signal of the complex PLL whose input is $v^{hf}_{dqhf\_s}$ , is obtained as the vector cross-product of the input signal and the estimated unit vector $e^{j\hat{\varphi}_{v^{hf}_{dqhf}}}$ , the resulting error (21) being function of the phase error between the actual high frequency voltage vector phase and its estimated phase ( $\hat{\varphi}_{v^{hf}_{dqhf}}$ ).

$$\varepsilon = v^{hf}_{dqhf} \times e^{j\hat{\varphi}_{v^{hf}_{dqhf}}} = \left|v^{hf}_{dqhf}\right| \sin(\hat{\varphi}_{v^{hf}_{dqhf}} - \hat{\varphi}_{v^{hf}_{dqhf}}) \tag{21}$$

- The output of the PLL's PI regulator is the estimated frequency of the input voltage vector ( $\hat{\omega}_{v^{hf}_{dqhf}}$ ), which is equal to the estimated machine speed in electrical units (see Fig. 4). Finally, $\hat{\varphi}_{v^{hf}_{dqhf\_s}}$ , is obtained by integration of the frequency

A different approach for the sensorless control of DFIG's injecting a high frequency signal voltage in the rotor was proposed in [32], the phase shift between the injected high frequency rotor voltage (instead of the high frequency rotor current), and the resulting high frequency stator voltage, was used in this case. However, estimating the rotor position using these two quantities requires the knowledge of the high frequency impedance phase angle $\varphi_{Z_{hf}}$ (16) as well as the equivalent impedance of the machine, brushes and grid. In [32] it was assumed that $\varphi_{Z_{hf}} = \pi/2$ . However, this assumption might not always be correct. Though it can be assumed that

$$(r_s + r_g) << (\omega_{hf} \pm \omega_r)(L_{ls} + L_g + L_m) \tag{22}$$

and

$$r_g << (\omega_{hf} \pm \omega_r)L_g \tag{23}$$

it is not straightforward to reach general conclusions on the value of $r_b^{'}$ , since it can change with the speed of the machine, brush temperature or other ambient conditions. Fig. 5 shows the measured high frequency resistance of the brushes for the test machine (see Table I), as a function of the speed. It can be observed that the high frequency resistance is significantly larger when the machine is at stand still, its value at rotor speeds different from zero being almost independent from the speed.

Table I Motor Parameters

| $U_{RATED}$ (V) (Stator) | $U_{RATED}$ (V) (Rotor) | $I_{RATED}$ (A) (Stator) | $I_{RATED}$ (A) (Rotor) | $f_{RATED}$ (Hz) |
|---|---|---|---|---|
| 380 | 190 | 12.5 | 25 | 50 |
| $P_{RATED}$ (kW) | $\omega_{RATED}$ (rpm) | $r_s$ (Ω) | $L_{ls}^{'}$ (mH) | $r_r^{'}$ (Ω) |
| 7.5 | 1500 | 0.416 | 5 | 0.75 |
| $L_{lr}^{'}$ (mH) | $L_m$ (mH) | $J$(Kgm$^2$) | | |
| 5.2 | 125.4 | 0.071 | | |

It is finally noted that one of the major limitations of saliency tracking based sensorless control techniques using high frequency signal injection [22-26] is their sensitivity to saturation induced and other secondary saliencies. However, as the method proposed in this paper doesn't track spatial saliencies but estimates the phase shift between the rotor high frequency current vector and the resulting stator high frequency voltage vector, it is not affected in principle by such effects.

## IV. High frequency signal injection

Implementation of the proposed method requires selection of the high frequency signal magnitude $V_{hf}$ and frequency $\omega_{hf}$ . Generally speaking, it is desirable to keep the magnitude as small as possible. The magnitude will be limited in first instance by connection standards [33], since the high frequency current resulting from the high frequency voltage induced in the stator might increase the THD, having therefore a negative impact on the power quality. In addition, if a large number of DFIG's relatively close to each other inject the high frequency signal simultaneously, interference might occur, strategies to avoid interference between DFIG's might then be needed. Deeper analysis of this issue is the subject of ongoing research.

Several issues need to be considered for the frequency selection:

- The maximum frequency is the Nyquist frequency (half of the switching frequency). In general, higher frequencies would be preferred, since they provide higher spectral separation from the fundamental component, which makes filtering easier [35].
- From the machine perspective, an inductive behavior was assumed in section III, higher carrier frequencies would boost the effect of the inductive terms over the resistive terms, therefore making this assumption safer. Fig. 6 shows the high frequency impedance of the test machine for three different frequencies, confirming the previous assumptions.

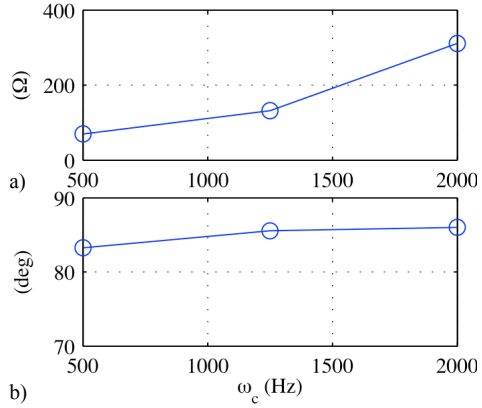


Fig. 6 High frequency impedance magnitude a) and phase b), of the test machine for different frequencies of the injected high frequency signal.

- The high frequency signal could interact with the grid resonance frequency, which can vary in a large range depending on the grid topology and transmission lines [33], also the ratio $r_g/L_g$ of the grid being function of this. It is therefore difficult to reach general conclusions in this regard.

## V. Simulation results

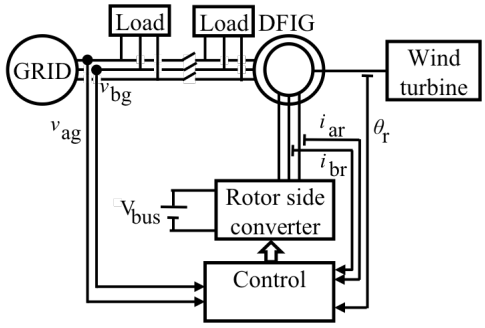


Fig. 7 Simulation setup.

The proposed sensorless control strategy was first tested by means of simulation, *DigSILENT PowerFactory* and the scenario shown in Fig. 7 were used for this purpose. The wind turbine power and machine speed changing, the model parameters being shown in Table II.

Fig. 8 shows the simulated response to step like changes of the wind speed from zero to 0.16 pu and 0.36 pu respectively, with the rotor $q$-axis current and the rotor speed responding as shown in Fig. 8a and 8b respectively. An MPPT strategy was used to select the operating points of the DFIG. Fig. 8c shows the phase error estimated from the injected high frequency signal voltage using the signal processing described in section III.

It is observed from Fig. 8c that the steady state error is negligible, the maximum transient error being <2deg. Transient errors are primarily due to the dynamic response of the filters used for the signal processing, including band-stop filters, band-pass filter and PLL (see Fig. 4). It is noted however that such transient effects should be of reduced importance in practice, as the large inertia of the wind turbine will smooth the changes in the actual speed [36].

| Table II Simulation Parameters | | |
|---|---|---|
| DFIG | | HF signal & signal processing |
| $U_{RATED}$ (Stator) = 380 V | $r_s$ = 0.164 Ω | $V_{hf}$ = 9.5 V (0.05 pu) |
| $U_{RATED}$ (Rotor) = 190 V | $L_{ls}$ = 5 mH | $\omega_{hf}$ = 500 Hz |
| $I_{RATED}$ (Stator)= 12.5 A | $r_r'$ = 0.75 Ω | PI Gain Kp = 70 |
| $I_{RATED}$ (Rotor)= 25 A | $L_{lr}$ = 5.2 mH | PI Gain Ki = 1.6 |
| $f_{RATED}$ = 50 Hz | $L_m$ = 125.4 mH | BS Filter BW = 20 Hz |
| $P_{RATED}$ = 7.5 kW | $J$ = 125.4 Kgm$^2$ | BP Filter BW = 10 Hz |
| $\omega_{RATED}$ = 1500 rpm | | |

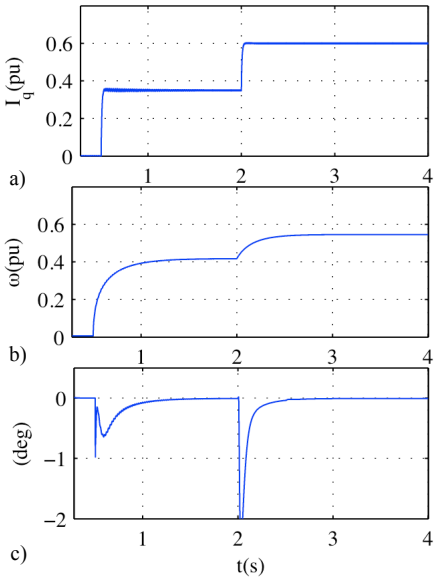


Fig. 8 Simulation results. Injected $I_q$ rotor current, a), machine speed, b) and position error, c). $V_{hf}$=0.05pu, $\omega_{hf}$=500Hz.

## VI. Experimental results

Experimental results showing the validity of the proposed method are presented in this section. The experimental setup is shown in Fig. 9, with the parameters of the test machine being shown in Table I. The short-circuit power of the grid is 2MVA, with

$r_g / X_g \approx 0.1 @ 50Hz$. The wind turbine (see Fig. 1) is emulated by means of a vector controlled IM, where a torque vs. speed curve providing MPPT of the wind turbine was used (see Fig. 14).

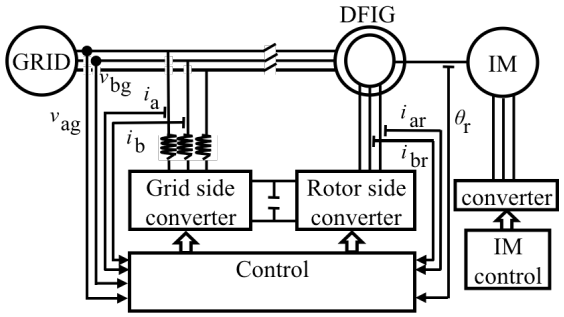


Fig. 9 Experimental setup.

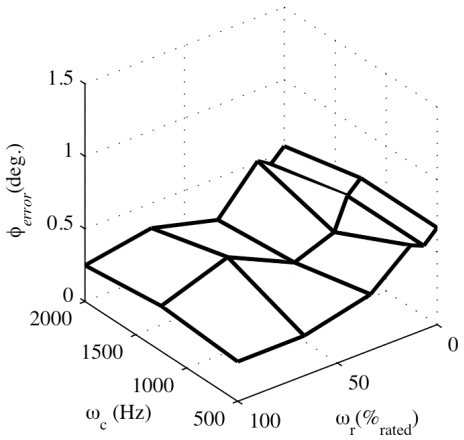


Fig. 10 Steady state error in the estimated rotor position when the DFIG is not connected to the grid. $V_{hf}$=5% of the line-to-line voltage, $I_d$=0pu, $I_d$=0pu.

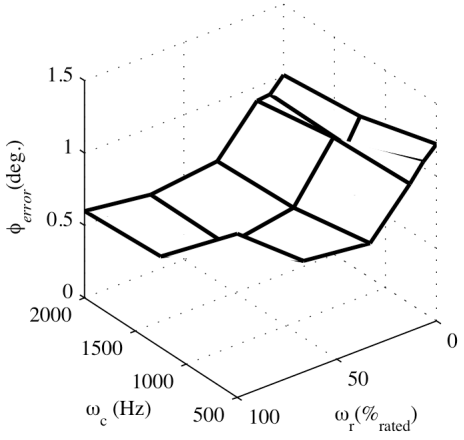


Fig. 11 Error in the estimated rotor position when the DFIG is connected to the grid. $V_{hf}$=5% of the line-to-line voltage, $I_d$ =0pu, $I_q$ =0pu.

Fig. 10 shows the steady state error in the estimated rotor position for different frequencies of the injected signal and machine speeds when the machine is not connected to the grid (see Fig. 9), the error is always smaller than 1 deg. As no stator current flows in this working condition, the phase shift between the rotor high frequency current and the induced stator high frequency voltage vector mainly depends on the high frequency magnetizing inductance ( $L_m$ ) of the machine.

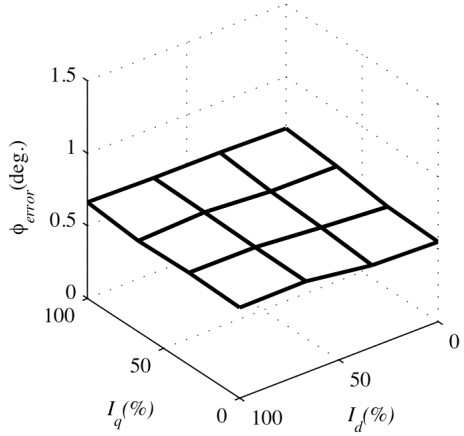


Fig. 12 Error of the estimated position for different d- and q-axis rotor current, and the DFIG connected to the grid. $V_{hf}$=5% of the line-to-line voltage, $\omega_{hf}$=2 kHz and $\omega_r$=40 Hz.

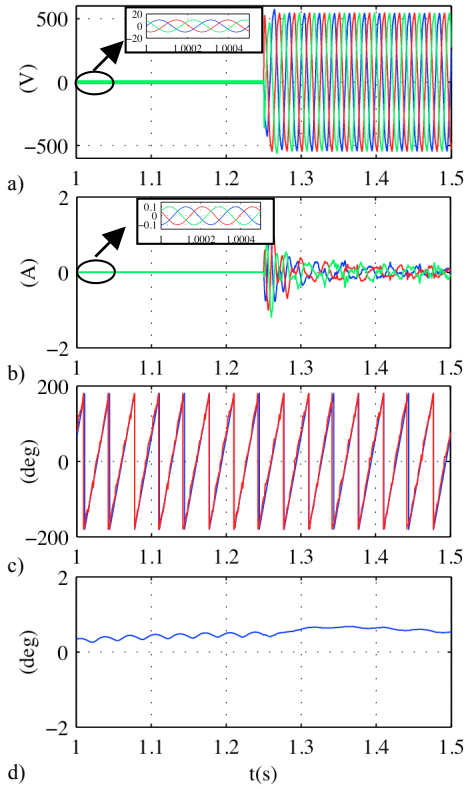


Fig. 13 Transient response when the DFIG is connected to the grid (t=1.25s). a) Stator phase voltages, b) rotor phase currents, c) estimated rotor position (bue) and measured rotor position (red) and d) estimated position error. $V_{hf}$=5% of the line-to-line voltage, $\omega_{hf}$=2kHz and $\omega_r$=30Hz.

Fig. 11 shows the same result as in Fig. 10 when the machine is connected to the grid, with the fundamental current commands, $I_d$ and $I_q$, being equal to zero. A slight increase of the estimated position error is observed for this case. This is due to the high frequency current flowing from the stator to the grid, meaning that the phase shift between

the rotor high frequency current and the induced stator high frequency voltage now depends on both the stator and grid high frequency impedances.

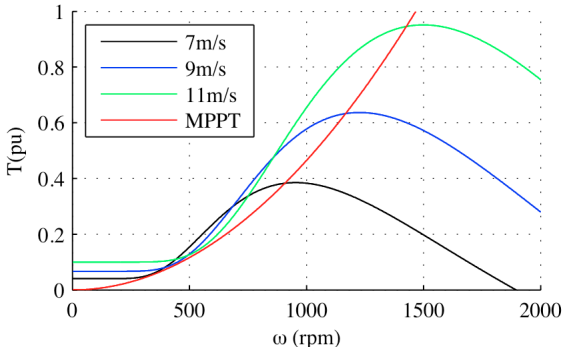


Fig. 14 Toque vs. speed characteristic of the wind turbine and MPPT characteristic of the DFIG.

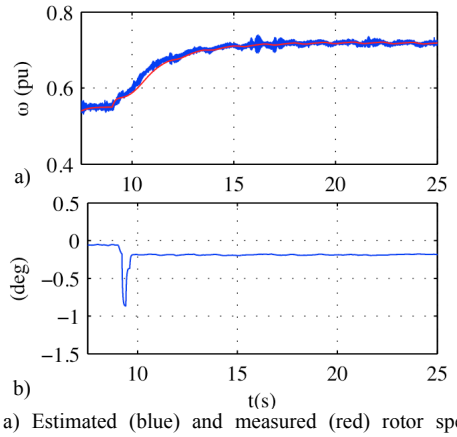


Fig. 15 a) Estimated (blue) and measured (red) rotor speed and b) position error. Wind speed change form 7 to 9 m/s, $V_{hf}$=5% of the line-to-line voltage and $\omega_{hf}$=2kHz.

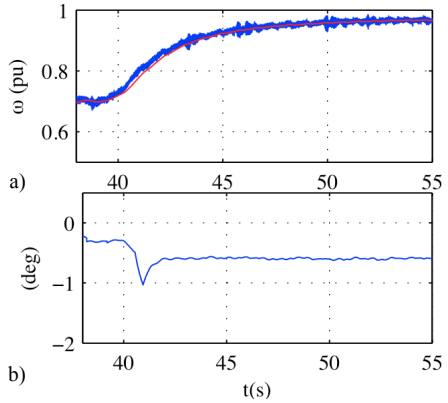


Fig. 16 a) Estimated (blue) and measured (red) rotor speed, and b) position error. Wind speed change form 9 to 11 m/s, $V_{hf}$=5% of the line-to-line voltage and $\omega_{hf}$=2kHz.

Fig. 12 shows the error of the estimated rotor position with the machine operating at constant speed for different values of the *d* and *q*-axis currents. It can be observed that the changes in the working condition have reduced impact on the estimated rotor position error.

Fig. 13 shows the transient response when the DFIG is connected to the grid, with the machine operated at constant speed and the high frequency signal voltage being injected continuously. It can be observed that before the DFIG is not connected to the grid (t<1.25s) (see Fig. 13a and 13b), only the rotor high frequency currents (Fig. 13b) and the stator high frequency voltage are present (Fig. 13a) while once the DFIG is connected to the grid (t>1.25s), both the fundamental and the high frequency signals are present. Fig. 13c shows the estimated and the measured rotor position while Fig. 13d shows rotor position error. It is observed that the mean position error is ≈0.35 deg. when the machine is not connected to the grid, increasing up to ≈0.90 deg. when the machine is connected to the grid, the absolute error being function of $(r_s + r_g)/(\omega_{hf} \pm \omega_r)(L_{ls} + L_g)$ for this case.

Finally, experimental results emulating the operation of a wind turbine controlled using MPPT for various working conditions are shown in Fig. 14 to 16. Fig. 14 shows the MPPT characteristic of the DFIG and the torque vs. speed characteristic of the wind turbine for different values of the wind speed. To emulate the wind turbine, its characteristics curves are programmed in the IM converter control (See Fig. 9). The high pass filters bandwidths (see Fig. 4) were set to 200Hz for both current and voltage complex vectors, the low pass filter for the current complex vector was set to 50Hz, the bandwidth for the complex PLL also being adjusted to 50Hz. Fig. 15 and 16 show the experimental results of a step change of the wind speed command in the IM control system. Fig. 15a shows the estimated and the measured rotor speed of the machine when a wind step like change from 7 to 9 m/s is commanded to the IM control system, while Fig.15b shows the estimated position error. Fig. 16 shows the same experimental results but for a wind step like change from 9 m/s to 11m/s, a similar behavior as for the previous case is observed. It is observed from Fig. 15b and 16b that there is a slight increase of the transient position error when the step commands are applied. However, as already stated, this effect should be of little importance in practice in real wind turbines, due to their large mechanical inertias.

## VII. Conclusions

This paper proposes the use of a high frequency signal injection method for the sensorless control of DFIG for wind power generation. While the physical principles are the same as for the case of other types of inverter fed three-phase AC machines like PM's and IM's, significant differences exist due to the fact that the rotor windings are accessible and that the stator windings are directly connected to the grid. The high frequency model of a DFIG has been derived from the fundamental model. Using this model, the physical principles of the method have been

established, and the signal processing needed to estimate the rotor position from the phase shift between the rotor high frequency current vector and the resulting stator high frequency voltage complex vector has been defined. Experimental results have been provided to confirm the viability of the proposed method.

Finally, the computational requirements of the proposed method are relatively small, meaning that it can be easily integrated in already existing digital signal processors.

## VIII. References


[1] Wind power Observatory, 2011. Available: www.aeeolica.org.

[2] The Spanish Electricity System Summary, 2010, REE, Madrid, Spain. Available: www.ree.es.

[3] Spain's National Renewable Energy Action Plan 2011-2020, Spanish ministry of industry, tourism and trade. Available: http://ec.europa.es/energy.

[4] A. Luna, F. K. A. Lima, D. Santos P. Rodriguez, E. H. Watanabae and S. Arnaltes, "Simplified Modeling of a DFIG for Transient studies in Wind Power Applcations," IEEE Trans. Ind. Elec., vol. 58 (1), pp. 9-20, Jan. 2011.

[5] "PO-12.3 Requisitos de respuesta frente a huecos de tension de las instalaciones eólicas", Spanish National Energy Commission, Oct. 2006.

[6] M. Tsili and S. Papathanassiou, "A review of grid code technical requirements for grid farms", IET Renew. Power Gen., vol. 3 (3), pp.308-332, Sep. 2009.

[7] "Wind turbines connected to grids with voltaged below 100kV", Transmission Lines Department (Denmark), Technical Regulations T.F. 3.2.6, May. 2004. Avalibale: www.wt-certification.dk.

[8] F. Santjer, G. J. Gerdes, P. Christiansen and D. Milborrow, "Wind turbine grid connection and interaction", DeuschesWindenergie-Institute GmbH, Tech-wise A/S and DM energy. Available: http://ec.europa.es/energy.

[9] S- Muller, M. Deicke and R. W. D. Donker, "Doubly Fed Induction Generation Systems for Wind Turbines", IEEE Ind. Appl. Mag., vol. 8 (3), pp. 26-33, May/June 2002.

[10] S. Yang and V. Ajjarapu, "A Speed-Adaptive Reduced-Order Observer for Sensorless Vector Control of Doubly Fed Induction Generator-Based Variable-Speed Wind Turbines", IEEE Trans. Energy Conv., vol. 25 (3), pp. 891-900, Sept. 2010.

[11] R. Pena, J.C. Clare and G. M. Asher, "Doubly Fed Induction Generator Using Back-to-Back PWM Converters and its Application to Variable Speed Wind Energy Conversion", IEE Proc. Elect. Power Appl., vol. 143 (5), pp.380-387, Sept. 1996.

[12] R. Cardenas, R. Peña, J. Proboste, G. Asher and J. Clare, "MRAS Observer for Sensorless Control of Standalone Doubly Fed Induction Generators", IEEE Trans. Energy Conv., vol. 20 (4), pp.710-718, Dec. 2005.

[13] B. Hopfensperger, D. J. Atkinson and R. A. Lakin, "Stator-Flux-Oriented Control of a Doubly-Fed Induction Machine with and without Position Encoder", IEEE Proc.-Electr. Power Appl., vol. 146 (4), pp.241-250, June 2000.

[14] F. K. A. Lima, A. Luna, P. Rodriguez, E. H. Watanabe and F. Blaabjerg, "Rotor Voltage Dynamics in Doubly Fed Induction Generator During Grid Faults", IEEE Trans. Power Elect., vol. 25 (1), pp.118-130, Jan 2010.

[15] B. Shen, B. Mwinyiwiwa, Y Chang and B.T. Ooi "Sensorless Maximum Power Point Tracking of Wind by DFIG Using Rotor Position Phase Lock Loop (PLL)", IEEE Trans. Power Elect., vol. 24 (4), pp.942-951, Apr. 2009.

[16] S. Z. Chen, N. C. Cheung, Y. Zhang, M. Zhang and X M Tang "Improved Grid Synchronization Control of Doubly Fed Induction Generator Under Unbalanced Grid Voltage", IEEE Trans. Energy Conv., vol. 23 (3), pp.799-810, Sept. 2011.

[17] L. A. de S. Ribeiro, M.C. Harke, and R.D. Lorenz, "Dynamic Properties of Back-emf Based Sensorless Drives," IEEE-IAS'06, Vol. 4, pp. 2026 - 2033, Oct 2006.

[18] P. P. Acarnely and j. F. Watson, "Review of Position-Sensorless Operation of Brushless Permanent-Magnet Machines," IEEE Trans. Ind. Electron., vol. 53 (2), pp.352-362, Apr. 2006.

[19] M. Schroedl, "Sensorless control of AC machines at low speed and standstill based on the 'INFORM' method," IEEE-IAS'96, vol. 1, pp. 270–277, 1996.

[20] S. Ogasawara and H. Akagi, "Approach to real-time position estimation at zero and low speed for a PM motor based on saliency," IEEE Trans. Ind. Applicat., vol. 34, pp. 163-168, Jan.-Feb. 1998.

[21] J. Holtz and H. Pan, "Acquisition of rotor anisotropy signals in sensorless position control systems," IEEE Trans. Ind. Appl., Sept./Oct. 2004, Vol. 40 (5), pp. 1379–1387.

[22] P.L. Jansen and R.D. Lorenz, "Transducerless position and velocity estimation in induction and salient AC machines," IEEE Trans. Ind. Appl., Vol. 31, pp. 240–247, Mar./Apr. 1995.

[23] P. García, F. Briz, M.W. Degner, D. Díaz-Reigosa, "Accuracy and Bandwidth Limits of Carrier Signal Injection-Based Sensorless Control Methods", IEEE Trans. Ind. Appl., Vol. 43 (4), pp. 990–1001, July/Aug. 2007.

[24] D. Reigosa, P. García, D. Raca, F. Briz, and R.D. Lorenz, "Measurement and Adaptive Decoupling of Cross-Saturation Effects and Secondary Saliencies in Sensorless-Controlled IPM Synchronous Machines," IEEE Trans. Ind. Appl., Vol. 44 (6), pp. 1758–1768, Nov./Dec. 2008.

[25] D. Reigosa, P. García, F. Briz, D. Raca and R.D. Lorenz, "Modeling and adaptive decoupling of transient resistance and temperature effects in carrier-based sensorless control of PM synchronous machines". IEEE Trans. Ind. Appl., Vol. 46 (1), pp. 139–149, Jan./Feb. 2010.

[26] D. Raca, P. García, D. Reigosa, F. Briz, and R.D. Lorenz, "Carrier Signal Selection for Sensorless Control of PM Synchronous Machines at Very Low and Zero Speeds," IEEE Trans. Ind. Appl., Vol. 46 (1), pp. 167–178, Jan./Feb. 2010.

[27] W. Hammel and R. M. Kennel, "Integration of alternating Carrier Injection in Sensorless Control Without any Filtering," IEEE Trans. Ind. Appl., Vol. 47 (3), pp. 1361–1379, May/June 2011.

[28] Y. Yoon, S. Sul, S. Morimoto and K. Ide, "High Bandwidth Sensorless Algorithm for AC Machines Based on Square-wave Type Voltage Injection," IEEE Trans. Ind. Appl., Vol. 47 (3), pp. 1361–1379, May/June 2011.

[29] C. Caruana, G. M. Asher and M. Sumner, "Performance of HF Signal Injection Techniques for Zero-Low_Frequency Vector Control of Induction Machines Under Sensorless Conditions," IEEE Trans. Ind. Elect., Vol. 53 (1), pp. 225–238, Feb. 2006.

[30] M. W. Degner and R. D. Lorenz, "Position Estimation in Induction Machines Utilizing Rotor Bar Slot Harmonics and Carrier Frequency Signal Injection," IEEE Trans. Ind. Appl., Vol. 36 (3), pp. 736–742, May/June 2000.

[31] J. I. Ha and S. K. Sul, "Sensorless Field-Oriented Control of an Induction Machine by High Frequency Signal Injection," IEEE Trans. Ind. Appl., Vol. 35 (1), pp. 45–51, Jan./Feb. 1999.

[32] L. Xu, E. Inoa, Y Liu and B. Guan, "A New High Frequency Injection Method for Sensorless Control of Doubly-Fed Induction Machines," IEEE ECCE'11, pp. 1758–1764, Sep. 2011.

[33] D. Reigosa, F. Briz, C. Blanco, P. García and J. M. Guerrero, "Islanding Detection Using High Frequency Signal Injection," IEEE ECCE'11, pp. 2183–2190, Sep. 2011.

[34] D. W. Novotny and T. A. Lipo, "Vector Control and Dynamics of AC Drives," Oxford Science Publications, 1996.

[35] D. Reigosa, F. Briz, M.W. Degner, P. García and J. M. Guerrero, "Temperature Issues in Saliency-Tracking Based Sensorless Methods for PM Synchronous Machines," IEEE Trans. Ind. Appl., Vol. 47 (3), pp. 1352–1360, May 2011.

[36] J. Morren, S. W. H. de Haan, W.L. Kling and J. A. Ferreira, "Wind Turbines Emulating Inertia and Supporting Primary Frequency Control," IEEE Trans. Power Sys., Vol. 21 (1), pp. 433–434, Feb. 2006.